Chemical Engineering Journal 522 (2025) 167732

Contents lists available at ScienceDirect

Chemical Engineering Journal

journal homepage: www.elsevier.com/locate/cej

Modulation of the *d*-band center through strong metal-support interaction with Ru and Cu_3P-MoP for efficient hydrogen oxidation

Shuqing Zhou [a,b], Yi Liu [a], Chenggong Niu [a], Jingya Guo [a,*], Tayirjan Taylor Isimjan [c,*], Jianniao Tian [a], Xiulin Yang [a,*]

[a] Guangxi Key Laboratory of Low Carbon Energy Materials, School of Chemistry and Pharmaceutical Sciences, Guangxi Normal University, Guilin 541004, China
[b] Guangxi Key Laboratory for Green Processing of Sugar Resources, College of Biological and Chemical Engineering, Guangxi University of Science and Technology, Liuzhou 545006, China
[c] Saudi Arabia Basic Industries Corporation (SABIC) at King Abdullah University of Science and Technology (KAUST), Thuwal, 23955-6900, Saudi Arabia

ARTICLE INFO

Keywords:
Metal-organic framework
Yolk-shell structure
Hydrogen oxidation reaction
D-band center
Catalytic mechanism

ABSTRACT

Constructing strong metal-support interaction (SMSI) to optimize the *d*-band center of materials is crucial for designing highly efficient hydrogen oxidation reaction (HOR) electrocatalysts. Herein, we propose a metal-organic framework (MOF) self-sacrificial pyrolysis-reduction strategy, which anchors Ru nanoparticles onto the folded Cu_3P-MoP ortho-octahedra (Ru/Cu_3P-MoP). The yolk-shell structure of Ru/Cu_3P-MoP catalyst exhibits remarkable mass activity of 2.49 mA μg_{Ru}^{-1}, respectively, significantly surpassing that of state-of-the-art Pt/C (0.18 mA μg_{Pt}^{-1}) and other comparative catalysts. Notably, the Ru/Cu_3P-MoP demonstrates commendable resistance to CO and stability, attributes that are lacking in Pt/C. Experimental results and density functional theory (DFT) calculations indicate that the SMSI between Ru and Cu_3P-MoP effectively modulates the *d*-band center of Ru/Cu_3P-MoP, which facilitates the optimal adsorption kinetics of hydrogen and hydroxyl groups and expedite the oxidation of CO, resulting in remarkable HOR reactivity and CO tolerance, thereby optimizing the adsorption energy of the reaction intermediates. Using life cycle analysis (LCA) and technoeconomic analysis (TEA) to compare Ru/Cu_3P-MoP with Pt/C, LCA shows Ru/Cu_3P-MoP has 27 % lower lifecycle emissions. TEA reveals an 87 % cost reduction and 22-fold better cost-per-performance, making it a superior alternative for alkaline fuel cells.

1. Introduction

Hydrogen conversion to electrochemical energy is emerging as a potential solution to address the global energy crisis and environmental degradation challenges [1]. While proton exchange membrane fuel cells (PEMFCs) have long been integral to these fields, alkaline exchange membrane fuel cells (AEMFCs) are rapidly gaining traction and are expected to emerge as viable alternatives to PEMFCs [2]. This shift is largely driven by advancements in anion-exchange membranes and the development of high-efficiency oxygen reduction reaction (ORR) catalysts based on non-platinum-group metals (PGMs), positioning AEMFCs at the forefront of energy research [3]. Anodic HOR, as the half-reaction of AEMFCs, is the key to drive its operation. However, when the electrolyte changes from acidic to alkaline, even the most active PGM-based electrocatalysts will experience a two-order-of-magnitude decrease in the kinetics of the anodic HOR [4]. Therefore, the development of highly efficient Pt-free alkaline HOR electrocatalysts is a crucial but still challenging task.

Currently, it is widely acknowledged that the Volmer step ($H_{ad} + OH^- \rightarrow H_2O + e^-$) is the rate-determining step in alkaline HOR process [5]. As a result, the adsorption behavior of hydrogen (H_{ad}) and hydroxyl groups (OH_{ad}) becomes critical indicators for evaluating HOR performance, with their intensities directly correlating to catalytic activity [6]. Previous studies have discovered that Ru not only exhibits a hydrogen bond strength similar to that of Pt, but also possesses significantly superior oxygen affinity compared to Pt [7,8]. Furthermore, Ru is approximately one-third the cost of Pt, making it a compelling alternative. Unfortunately, pristine Ru suffers from severe deficiencies in intrinsic activity, resistance to CO poisoning, and long-term stability, rendering it challenging to achieve a short-term replacement for Pt [9]. To address these limitations, researchers have explored various strategies to modify Ru. According to the *d*-band center theory, optimizing the

* Corresponding authors.
E-mail addresses: jyguo@gxnu.edu.cn (J. Guo), isimjant@sabic.com (T.T. Isimjan), xlyang@gxnu.edu.cn (X. Yang).

https://doi.org/10.1016/j.cej.2025.167732
Received 23 April 2025; Received in revised form 31 July 2025; Accepted 24 August 2025
Available online 25 August 2025
1385-8947/© 2025 Elsevier B.V. All rights are reserved, including those for text and data mining, AI training, and similar technologies.

d-band center of catalyst to regulate the intermediates adsorption is an effective means to enhance HOR performance [10]. Studies indicate that approaches such as elemental doping [11], alloying [12], and defect engineering [13] an successfully adjust the *d*-band center. Notably, strong metal-support interactions (SMSIs) offer a powerful and precise approach for *d*-band center engineering, significantly boosting intrinsic activity and durability [14]. For instance, Yu et al. demonstrated that an N-$SrMoO_4$ support interacting with Ni_4Mo induced a downshifted *d*-band center and thermoneutral H* adsorption, dramatically enhancing HOR performance [15].

Transition metal phosphides (TMPs) are particularly attractive SMSI supports due to their tunable electronic structures and good conductivity [16,17]. However, conventional SMSI strategies often rely on single-component supports (e.g., carbon, metal oxides, or single TMPs, which frequently face inherent trade-offs or limitations in simultaneously optimizing the electronic structure of Ru, providing abundant active sites, ensuring high stability, and facilitating mass transport [18,19]. This challenge underscores the need for novel support design strategies to unlock the full potential of SMSIs for alkaline HOR.

To address this critical gap, we propose a novel strategy utilizing a metal-organic frameworks (MOFs)-derived bimetallic phosphide composite support (Cu_3P-MoP) to establish enhanced SMSIs for precise *d*-band center modulation of Ru nanoparticles. The rationale for selecting Cu_3P and MoP stems from their complementary electronic properties and anticipated synergistic effects at their interface, offering a unique platform to overcome the limitations of single-component TMP supports [20,21]. It can be expected that the internal electronic coupling within the Cu_3P-MoP composite will generate a more effective SMSI with Ru, enabling superior control over the d-band center position and interfacial environment to optimize both H* and OH* adsorption/desorption energetics, while concurrently enhancing stability and conductivity.

Herein, we had developed an efficient HOR catalyst with a large specific surface area by confining Ru nanoparticles on Cu_3P-MoP octahedra via a MOF self-sacrificial-pyrolysis strategy. Experimental findings revealed that the work function difference between Ru and Cu_3P-MoP led to the electronic reconstruction of the Ru/Cu_3P-MoP catalyst, thereby enhancing the interfaces water adsorption. Density functional theory (DFT) calculations further demonstrated that the strong metal-support interaction between Ru and Cu_3P-MoP optimized the catalyst's *d*-band center, facilitating the adsorption and desorption of H* and OH* intermediates and accelerating HOR kinetics. Consequently, the Ru/Cu_3P-MoP offered significant exchange current densities and mass activities that exceeded those of advanced Pt/C and contrastive samples. Remarkably, the Ru/Cu_3P-MoP catalyst demonstrated strong CO tolerance and stability, a feature lacking in Pt/C catalysts.

2. Experimental section

2.1. Chemicals

All chemicals and reagents were utilized as purchased without any further purification. These included copper acetate monohydrate ($Cu(CH_3COO)_2{\cdot}H_2O$, AR), phosphomolybdic acid hydrate ($H_3[P(Mo_3O_{10})_4]{\cdot}xH_2O$, AR]), trimesic acid-1,3,5-benzenetricarboxylic acid ($C_9H_6O_6$ (H_3BTC), AR), 3-Hydroxytyramine hydrochloride, ruthenium trichloride ($RuCl_3{\cdot}xH_2O$, ~40 wt% Ru), red phosphorus (P, AR), L-glutamic acid ($C_5H_9NO_4$, AR), ethylene glycol (EG, AR), commercial Pt/C (20 wt% Pt), nafion solution (5 wt%), and potassium hydroxide (KOH, AR). The deionized water (18.25 MΩ cm^{-1}) from a water purification system (Ulupure) was used throughout the whole experiment.

2.2. Synthesis of NENU-5 metal-organic framework (MOF) and Cu_3P-MoP

For the preparation of NENU-5, Solution A was first prepared by dissolving 1 g of copper acetate, 1.5 g of phosphomolybdic acid, and 0.35 g of L-glutamic acid in 100 mL of H_2O. Simultaneously, Solution B was prepared by dissolving 0.7 g of trimethylolpropionic acid in 100 mL of ethanol. Solution B was slowly added dropwise into Solution A while stirring at room temperature for 14 h. The resulting product was collected by centrifugation, washed three times with a 1:1 water/ethanol mixture (*v*/v), and dried overnight at 60 °C to yield NENU-5. To synthesize Cu_3P-MoP, the obtained NENU-5 was uniformly mixed with red phosphorus (P) in a 1:2 mass ratio through grinding. This mixture was then calcined in a nitrogen atmosphere at 950 °C (alternatively at 900 °C or 1000 °C) for 2 h, with a heating rate of 5 °C min^{-1}. After natural cooling, the product was collected and designated as Cu_3P-MoP, with temperature variants labeled as Cu_3P-MoP-900 or Cu_3P-MoP-1000.

2.3. Synthesis of Ru/Cu_3P-MoP

To prepare Ru/Cu_3P-MoP, 50 mg of Cu_3P-MoP was dispersed in a 40 mL mixture of H_2O and ethylene glycol (*v*/v = 1:1). Simultaneously, 12 mg (9 or 15 mg) of $RuCl_3$ was added to the dispersion. The mixture was ultrasonicated for 30 min and subsequently heated in an oil bath at 120 °C for 4 h. The product was collected via centrifugation, washed several times with water and ethanol, and vacuum-dried at 60 °C overnight to obtain Ru/Cu_3P-MoP. The synthesized samples were labeled as $Ru_{3.14}$/Cu_3P-MoP and $Ru_{6.26}$/Cu_3P-MoP based on their specific Ru content. The Ru content, determined by inductively coupled plasma mass spectroscopy (ICP-MS), was found to be 5.01 wt%. For comparison, additional samples labeled Ru/Cu_3P and Ru/MoP were synthesized following the same procedure.

2.4. Life cycle analysis (LCA)

The life cycle analysis (LCA) evaluates the environmental impact of the Ru/Cu_3P-MoP catalyst and compares it to the commercial Pt/C catalyst. The analysis considers key stages, including raw material extraction, synthesis, operational use, and recycling, quantifying greenhouse gas (GHG) emissions in terms of carbon dioxide equivalents (CO_2-eq). This holistic approach ensures a comprehensive understanding of the sustainability of these catalysts.

2.5. Techno-economic analysis (TEA)

The technoeconomic analysis (TEA) assesses the cost of producing and using Ru/Cu_3P-MoP compared to Pt/C, taking into account raw material costs, synthesis expenses, and performance-adjusted costs. This analysis provides insights into the economic feasibility of the catalysts for hydrogen oxidation applications.

3. Results and discussion

3.1. Synthesis and characterization

The Ru/Cu_3P-MoP composite was constructed using a MOF-assisted pyrolysis-reduction strategy, as schematically depicted in **Fig. 1**a (see Experimental section for details). Specifically, H_3BTC, $H_3[P(Mo_3O_{10})_4]$ and $Cu(CH_3COO)_2$ were first self-assembled to form octahedral NENU-5 at room temperature (**Fig. S1**a). Then, the NENU-5 was carburized at 950 °C for 2 h to convert into Cu_3P-MoP, alongside the reduction of Ru onto Cu_3P-MoP support's surface. The expected Ru content was 5.01 wt % verified by ICP-MS measurements. Literature indicated that MOF-derived materials' morphology is closely associated with the carbonization temperature, which can be further determined by thermogravimetric analysis (TGA) [22]. A TGA analysis was performed to investigate the decomposition behavior of the NENU-5 organic linker and its relationship to the carbonization temperature. In **Fig. 1**b, the weight loss of NUNE-5 below 265 °C was primarily due to the evaporation of absorbed water. The significant weight loss observed between 265 and 400 °C corresponded to the decomposition of the organic ligand and the

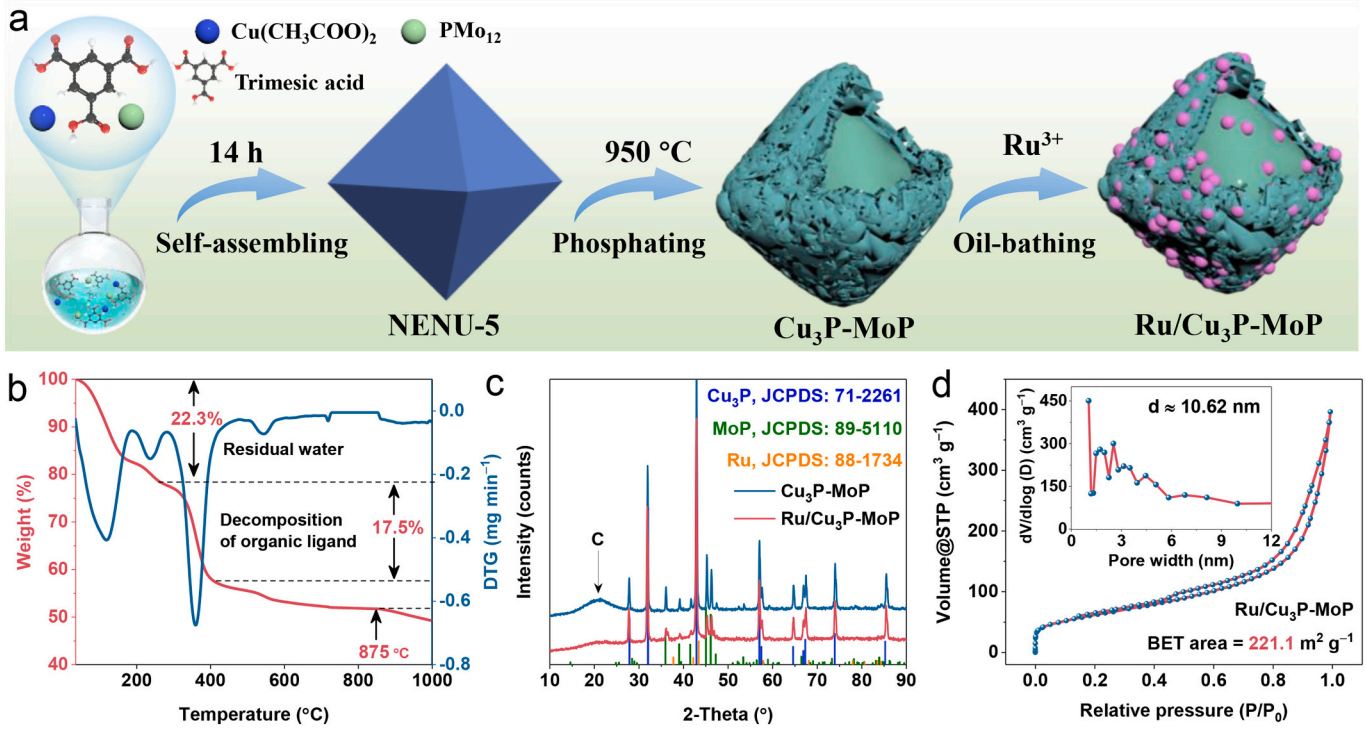

Fig. 1. (a) Schematic diagram of preparation of Ru/Cu_3P-MoP catalyst. (b) TGA measurement of NENU-5. (c) XRD patterns of Ru/Cu_3P-MoP and Cu_3P-MoP. (d) N_2 adsorption-desorption isotherms with the corresponding pore size distribution (inset) of Ru/Cu_3P-MoP.

conversion of metals to metal oxides. Further weight loss between 400 and 875 °C was associated with interactions between carbon and metal oxides [23]. Notably, interactions between carbon and metal oxides intensified at temperatures exceeding 875 °C, prompting us to phosphide the NUNE-5 organic linker within the 900–1000 °C. The X-ray diffraction (XRD) patterns for the Cu_3P-MoP, Ru/Cu_3P, Ru/MoP and Ru/Cu_3P-MoP catalysts were presented in Fig. 1c and **Figs. S1**b-c. The diffraction peaks for Cu_3P-MoP, Ru/Cu_3P, Ru/MoP and Ru/Cu_3P-MoP corresponded to the hexagonal Cu_3P (JCPDS: 71–2261) [24] or/and hexagonal MoP (JCPDS: 89–5110) [25], confirming the successful synthesis of Cu_3P-MoP support. The low amount of Mo_4P_3 observed in **Fig. S1**c originated from the violent volatilization of red phosphorus at elevated temperatures, which induced a localized or transient phosphorus deficiency, ultimately leading to the formation of this phosphorus-deficient intermediate phase [26]. Whereas the lack of diffraction peaks for Ru in these samples suggested its amorphous nature [23]. Brunauer-Emmett-Teller (BET) adsorption-desorption isotherm analysis revealed that the specific surface area of Ru/Cu_3P-MoP was 221.1 $m^2\ g^{-1}$ (Fig. 1d), with a pore size distribution centered around 10.62 nm, highlighting its mesoporous structure. This mesoporous material can function as catalyst supports, hosting active Ru nanoparticles within the pores, effectively preventing the agglomeration of Ru nanoparticles and increasing the accessibility of active sites [27].

To probe the microstructure of the catalysts, scanning electron microscopy (SEM) and transmission electron microscopy (TEM) were utilized. As depicted in Fig. 2a, NENU-5 exhibited a well-dispersed octahedral morphology with a smooth surface. TEM images of the Ru/Cu_3P-MoP catalyst revealed a distinctive yolk-shell hollow structure. Within this structure, the Cu_3P-MoP support formed the yolk. Benefiting from the synergistic effect between Ru and the Cu_3P-MoP support, Ru nanoparticles were uniformly anchored onto the carbon shell with an average particle size as low as ~1.67 nm (Figs. 2b-c and inset), significantly enhancing atomic utilization efficiency. In contrast, Ru tended to agglomerate on the single-component Cu_3P support, resulting in significantly larger surface nanoparticles (~3.88 nm, **Fig. S2**). This agglomeration likely covered numerous active sites, leading to inferior electrochemical performance compared to the Ru/Cu_3P-MoP catalyst. The yolk-shell structure offers dual advantages. It facilitates the rapid diffusion of H_2 molecules to the catalytic active sites, thereby enhancing the reaction rate and overall efficiency [5], and the synergistic interaction between the Cu_3P-MoP yolk and the Ru shell reduces the activation energy barrier, significantly improving the electrocatalytic performance [28]. High-resolution TEM (HR-TEM) images (Figs. 2d-f) further confirmed the successful fabrication of the Ru/Cu_3P-MoP hybrid. Lattice fringes with spacings of 0.281, 0.315, and 0.214 nm were observed, corresponding to the (100) plane of MoP, the (111) plane of Cu_3P, and the (002) plane of Ru, respectively. These observations were consistent with the XRD results, affirming the structural integrity of the Ru/Cu_3P-MoP catalyst. Additionally, high-angle annular dark-field scanning TEM (HAADF-STEM) combined with energy-dispersive X-ray (EDX) mapping revealed the uniform distribution of C, P, Cu, Mo, and Ru throughout the yolk-shell structure (Fig. 2g), further validating the catalyst's composition and architecture.

The surface constitution and chemical states of Ru/Cu_3P-MoP was investigated using X-ray photoelectron spectroscopy (XPS). The XPS survey spectrum (**Fig. S3**) confirmed the presence of C, P, Cu, Mo, and Ru in the Ru/Cu_3P-MoP composite. The high-resolution Ru 3*d* + C 1 *s* spectrum (Fig. 3a) calibrated at 284.0 eV was served as a standard reference.[25] Meanwhile, the deconvoluted peaks situated at around 280.19 and 281.32 eV indexed to metallic Ru and RuO_2, respectively. Wherein the existence of RuO_2 stemmed from unavoidable air exposure [29]. In the Mo 3*d* XPS spectra (Fig. 3b), the deconvoluted peaks near 227.21 and 230.45 eV corresponded to Mo $3d_{5/2}$ and Mo $3d_{3/2}$, which were typical peaks of MoP [30]. The additional doublets peaks at 231.91 eV and 235.12 eV coincided with the high oxidation state of MoO_3 (Mo(VI)), consistent with previous reports [20]. Intriguingly, the binding energy of Mo—P in Ru/Cu_3P-MoP showed a positive shift of 0.16 eV compared to Cu_3P-MoP, suggesting a significant electronic interaction between Ru and the Cu_3P-MoP support [31]. As observed in Fig. 3c, the Cu 2*p* spectra was divided into four peaks at 931.74, 934.23,

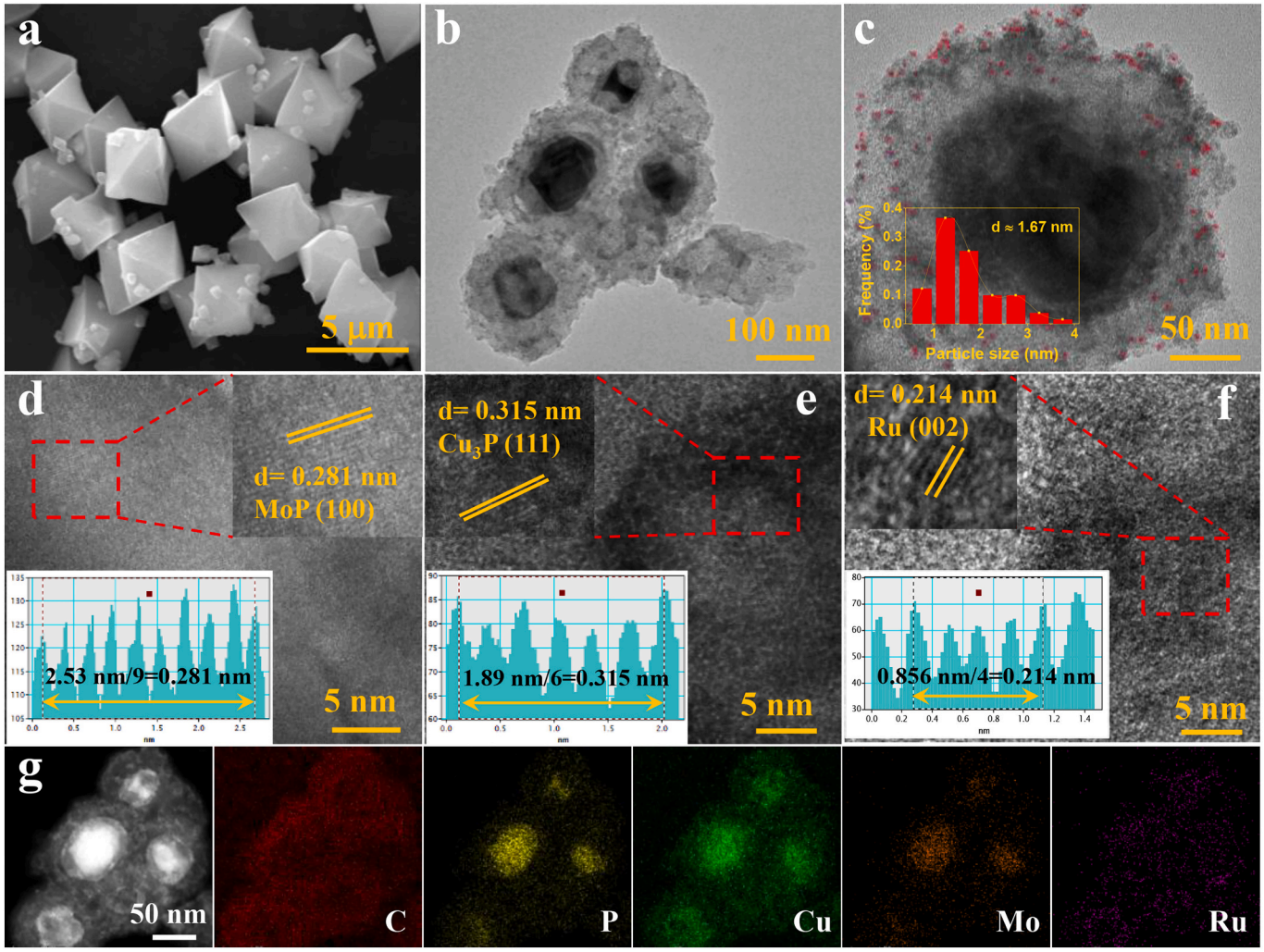

Fig. 2. (a) SEM image of NUNE-5. (b-c) TEM images of Ru/Cu_3P-MoP and corresponding particle size distribution. (d-f) High-resolution TEM images of Ru/Cu_3P-MoP. (g) C, P, Cu, Mo and Ru elemental mappings.

939.79 and 942.90 eV, matching the Cu—P and Cu—O bonds and two satellite peaks, respectively [32]. The binding energy of Ru/Cu_3P-MoP was negatively shifted by 0.1 eV compared to Cu_3P-MoP, indicating strong electronic interactions between Cu and other components. Furthermore, the Auger electron spectroscopy in **Fig. S4** also revealed the existence of Cu^+ species. The P 2*p* spectrum (Fig. 3d) of Ru/Cu_3P-MoP featured triple peaks near 129.17, 130.04, and 132.63 eV attributed to the $2p_{3/2}$ and $2p_{1/2}$ of the P-M and P—O bonds, respectively [33]. The binding energy of Ru/Cu_3P-MoP shifted positively by approximately 0.31 eV compared to Cu_3P-MoP, implying that partial electron transfer from metal-P to Ru facilitated a significant charge interconversion, resulting in electronic reconstruction at the metal center's surface, thereby enhancing the catalyst's mass transfer and reaction kinetics [34,35].

Moreover, ultraviolet photoelectron spectroscopy (UPS) measurements were conducted to access the material's work function (WF) and elucidate the surface electronic characteristics. The cutoff level (E_{cutoff}) of the catalyst was established and the work function was calculated, as shown in Fig. 3e. The WFs of Ru, Cu_3P-MoP and Ru/Cu_3P-MoP were determined to be 4.31, 2.50 and 4.74 eV, respectively. The higher WF of Ru/Cu_3P-MoP indicated that electrons were less likely to escape, suggesting that Ru readily accepted electrons from Cu_3P-MoP, leading to charge redistribution across the Ru/Cu_3P-MoP surface [36]. In addition, we established that the maximum valence bands for Ru, Cu_3P-MoP and Ru/Cu_3P-MoP were 3.54, 3.41 and 3.08 eV, respectively. Given that valence electrons close to the Fermi level make significant contributions to majority of *d* states. When compared with Cu_3P-MoP and Ru, the maximum valence bands of Ru/Cu_3P-MoP was closer to the Fermi level, suggesting its enhanced conductivity [37]. The energy band diagram was conceived based on catalyst's WF and valence band results, as depicted in Fig. 3f. Apparently, the optimization of Fermi level in the Ru/Cu_3P-MoP hybrid increased the charge accumulation at the complex interface while reducing species adsorption due to the pinning effect, which could favorably enhance the HOR kinetics [38]. The catalysts' wettability was assessed via liquid contact angle (CA) measurements. In Fig. 3g, the CA value of Ru/Cu_3P-MoP (29.8°) was lower than that of Ru/MoP (50.0°) and Ru/Cu_3P (57.1°), suggesting the preferable surface wettability and hydrophilicity of the Cu_3P-MoP heterostructure. This enhanced wettability allows the electrolyte to permeate easily into the pore structure, facilitating OH^- adsorption and expediting HOR kinetics [19].

3.2. Alkaline electrochemical properties

The rotating disk electrode (RDE) technique was employed to investigate the HOR electrocatalytic performance of the synthesized catalysts in an H_2-saturated 0.1 M KOH electrolyte. All electrochemical data were iR-corrected to account for solution resistance. Initially, we fine-tuned the pyrolysis temperature and Ru metal content to determine optimal synthesis conditions. As depicted in **Figs. S5–6**, the Ru/Cu_3P-

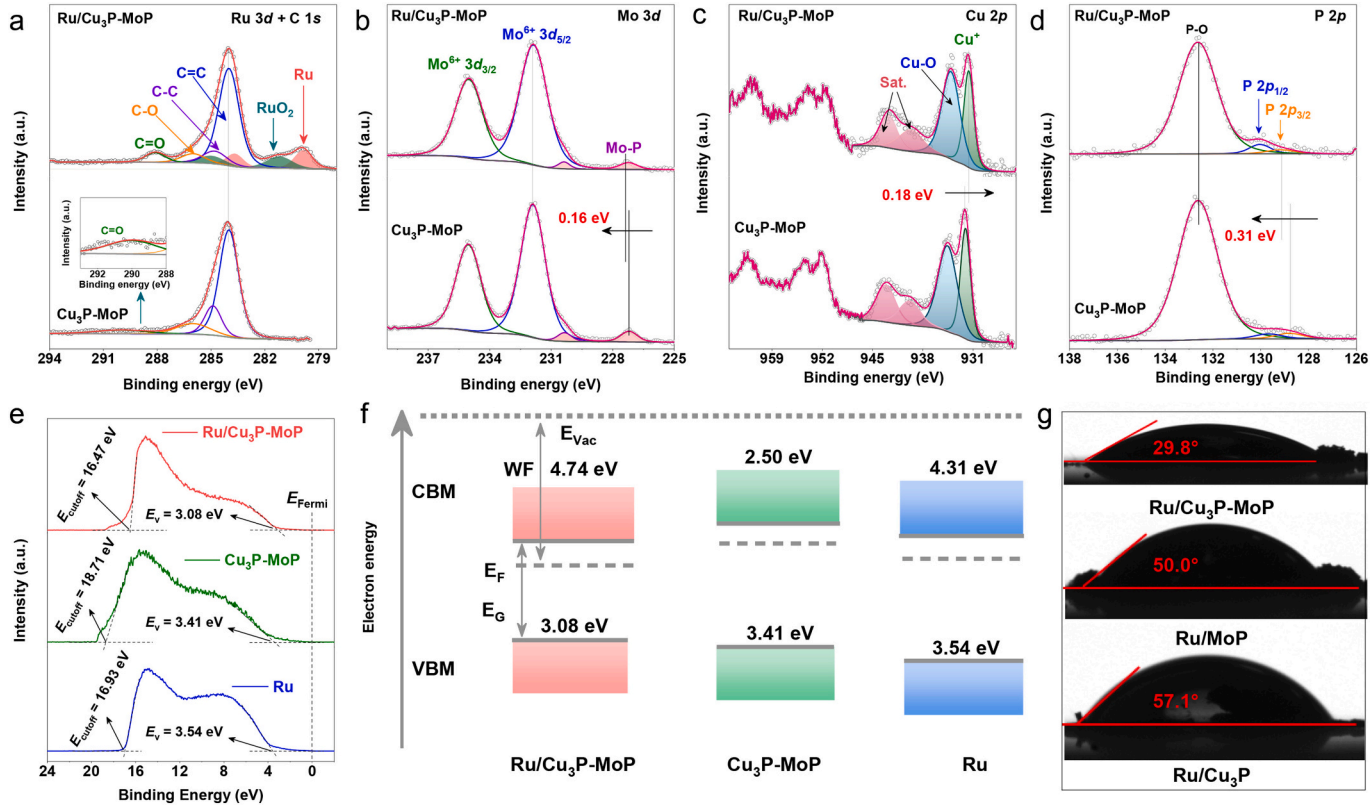

Fig. 3. High-resolution XPS spectra of (a) Ru 3*d* + C 1 *s*, (b) Mo 3*d*, (c) Cu 2*p* and (d) P 2*p*. (e) UPS spectra and (f) corresponding energy-band alignment diagram of Ru/Cu_3P-MoP, Cu_3P-MoP and Ru. (g) Bubble contact angle images of Ru/Cu_3P-MoP, Ru/MoP and Ru/Cu_3P.

MoP hybrid with a pyrolysis temperature of 950 °C and 5.01 wt% Ru content (**Table S4**) showcased peak HOR activity. Subsequently, the HOR activities of Ru/Cu_3P-MoP, Ru/Cu_3P, Ru/MoP, Cu_3P-MoP and commercial Pt/C were qualitatively evaluated. The polarization curves (Fig. 4a) revealed that Ru/Cu_3P-MoP displayed the highest anodic current density across the entire potential range. In contrast, Cu_3P-MoP showed minimal current response, highlighting the exceptional synergistic effects and electronic interaction between Ru nanoparticles and Cu_3P-MoP support in promoting the catalyst's reactivity for the HOR process. Moreover, the HOR polarization curve of Ru/Cu_3P-MoP in N_2-saturated electrolyte displayed ultra-low anodic current, indicating that the anodic current originated from H_2 oxidation (**Fig. S7**) [39]. The exchange current density (j_0) of these electrocatalysts was determined using the Butler-Volmer equation, which is proportional to the slope of the fitting curves in micropolarization region. (Figs. 4b and d). The j_0 of the Ru/Cu_3P-MoP was signally larger than those of Ru/Cu_3P, Ru/MoP and Pt/C, suggesting that it possessed remarkable inherent activity (**Table S5**) [40]. The kinetic currents density (j_k) derived from HOR polarization curves adopting the Koutecky−Levich equation. In Figs. 4c and d, Ru/Cu_3P-MoP displayed the highest j_k (25.43 mA cm^{-2}) among all the tested electrocatalysts, underlining its fastest HOR kinetics. To improve accuracy, we remeasured polarization curves at multiple rotation rates and constructed Koutecky–Levich plots to extract the intrinsic j_K value. The result (3.45 mA cm^{-2}) closely matches the original (4.14 mA cm^{-2}), confirming the reliability of our data (**Fig. S8**). To quantitatively evaluate the HOR activity of Ru/Cu_3P-MoP hybrid in comparison with Pt/C and other samples, the mass activity (MA) was further computed. As presented in Fig. 4e, the MA of Ru/Cu_3P-MoP was estimated to be 2.49 mA μg_{Ru}^{-1} at 50 mV, significantly surpassing documented noble metal catalysts (**Table S6**). Stability, a critical factor in evaluating catalysts, was assessed through accelerated durability and chronoamperometry tests. As displayed in Fig. 4f, a neglected decline in activity was observed after 1000 cycles of cyclic voltammetry (CV) testing. However, the severe deactivation of Pt/C catalysts after prolonged HOR cycling stems from an inevitable consequence of the synergistic and mutually reinforcing effects of Pt nanoparticle agglomeration, Pt dissolution/leaching, and carbon support corrosion (**Figs. S9–10**) [32,41,42]. As a stark contrast, the LSV polarization curve of Ru/Cu_3P-MoP was basically consistent with the initial curve, confirming its excellent stability. Furthermore, during chronoamperometry tests at a fixed potential, the current density of Ru/Cu_3P-MoP showed only a slight decrease after continuous operation for 20,000 s (Fig. 4g), further demonstrating its exceptional long-term stability. As demonstrated in **Fig. S11**, Ru/Cu_3P-MoP-After catalyst still preserved its pristine morphology except for some structural collapse. Simultaneously, we find that the Ru/Cu_3P-MoP-After still has Ru, Mo—P and Cu^+ signals, while the Cu—O signal was significantly enhanced, which was consistent with the theoretical results caused by the long-term H_2 oxidation process (**Fig. S12**).

Reportedly, the HBE and OHBE are widely recognized as key metrics for evaluating activity during the alkaline HOR process [43]. The hydrogen underpotential deposition (H_{upd}) peak in CV is directly associated with the HBE. And the smaller the peak potential in H_{upd} region, the weaker the HBE, which is more advantageous for the HOR process [44]. The double-layer capacitance of the studied catalyst within the non-faradaic potential window is small; therefore, the resulting capacitive current has a negligible influence on the HOR polarization curves, especially for kinetic analysis (**Fig. S13**). In Fig. 5a, the CV curves recorded in N_2-saturated 0.1 M KOH revealed that the H_{upd} peak potential of Ru/Cu_3P-MoP (0.182 V) was more negative than those of Ru/Cu_3P (0.198 V) and Ru/MoP (0.202 V), reflecting that Ru/Cu_3P-MoP boasted the superior HOR activity. Given that adsorbed OH^- species facilitate the removal of adsorbed CO intermediates from the metal surface, CO stripping voltammetry was performed to evaluate OH^- adsorption ability [45]. As exhibited in Fig. 5b, the CO oxidation peak of Ru/Cu_3P-MoP was around 0.780 V, clearly showing that Ru/Cu_3P-MoP

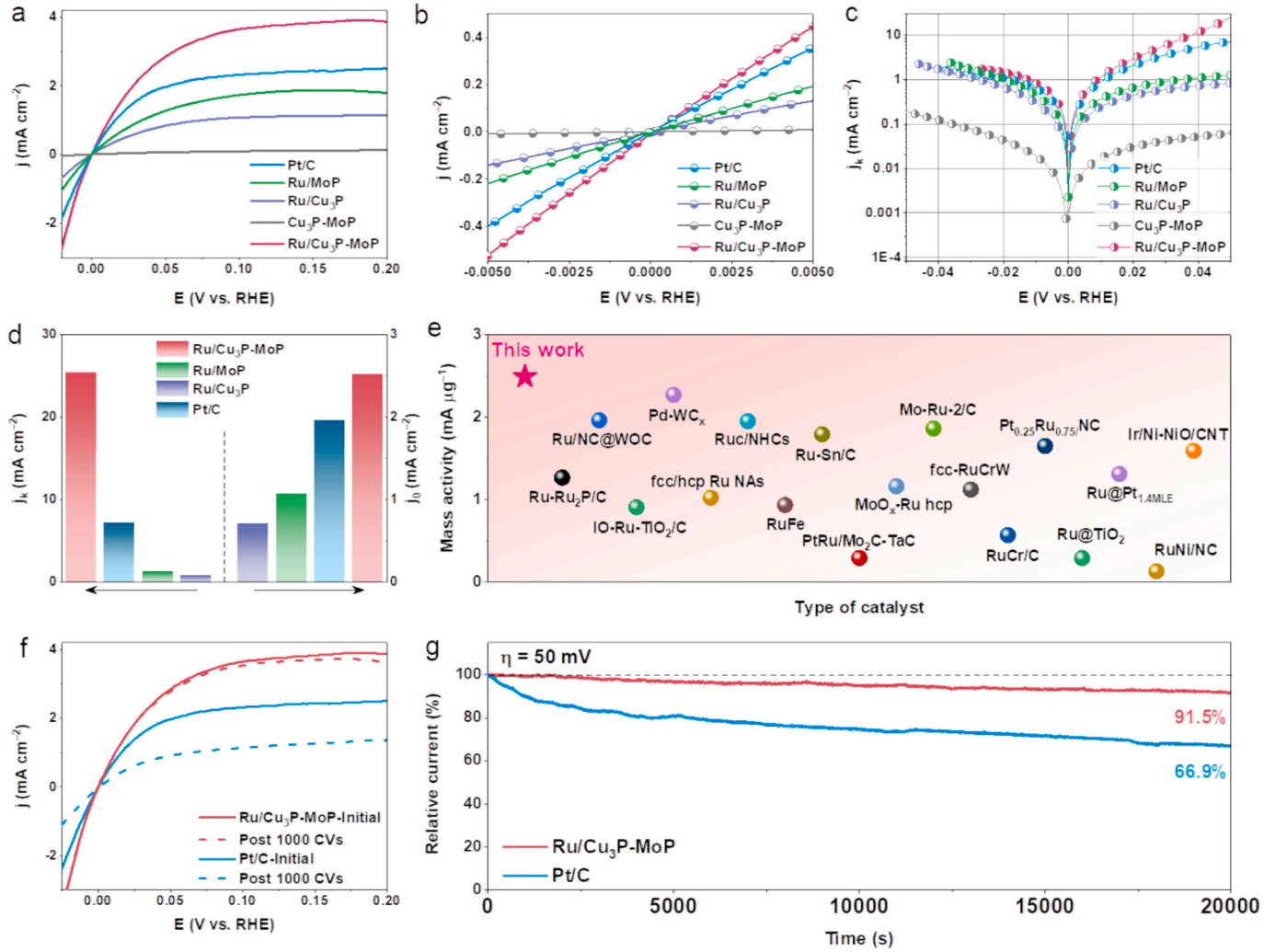

Fig. 4. (a) HOR polarization curves of different catalysts in H_2-saturated 0.1 M KOH with a rotation rate of 1600 rpm. (b) Tafel plots. (c) Linear fitting curves in micropolarization region. (d) Summarization of j_k and j_0 of studied catalysts. (e) Comparison of mass activity (MA) at 50 mV with previously reported alkaline HOR electrocatalysts. (f) HOR polarization curves before and after 1000 cycles and (g) chronoamperometric response at 50 mV of Ru/Cu_3P-MoP and commercial Pt/C.

had the strongest OH^- adsorption compared to Ru/Cu_3P (0.841 V) and Ru/MoP (0.818 V). This more negative CO stripping potential indicates optimized hydroxyl intermediate adsorption and an accelerated Volmer step, which are critical for enhancing alkaline HOR performance [46]. Additionally, the zeta potential of Ru/Cu_3P-MoP was measured to assess its surface charge and OH^- adsorption capability. Fig. 5c illustrated that the zeta potential of Ru/Cu_3P-MoP (−16.2 mV) was significantly lower than those of Ru/Cu_3P (−10.6 mV) and Ru/MoP (−13.2 mV), suggesting enhanced OH adsorption capacity [47]. Considering that crude hydrogen often contains trace amounts of CO, which can poison fuel cell systems, the CO tolerance of the samples was further investigated. As shown in Fig. 5d, Ru/Cu_3P-MoP maintained high HOR activity in an H_2-saturated 0.1 M KOH electrolyte containing 1000 ppm CO. In contrast, the activity of Pt/C decreased dramatically, demonstrating the superior CO tolerance of Ru/Cu_3P-MoP [48]. The enhanced HOR performance of Ru/Cu_3P-MoP originates from complex interfacial electronic effects that go beyond the predictive scope of a single *d*-band center descriptor [49,50]. The Cu_3P-MoP heterojunction induces strong local charge redistribution, forming a distinct electronic environment at the Ru sites. This modulates the hydrogen binding energy, making it weaker than in Ru/Cu_3P or Ru/MoP, despite an intermediate *d*-band center. Meanwhile, OH adsorption mainly occurs on the support, especially MoP-rich interfacial regions, consistent with the known OH affinity of Mo-based phosphides [51–53]. These findings support a bifunctional mechanism in which Ru facilitates H-related steps while the Cu_3P-MoP support activates OH species.

To further investigate the adsorption behavior of hydrogen ions (H^+) and the role of interfacial water in the hydrogen electrode reaction on the Ru/Cu_3P-MoP surface, in situ attenuated total reflection surface-enhanced infrared absorption spectroscopy (ATR-SEIRAS) analysis was performed. The relevant spectra were recorded in H_2-saturated 0.1 M KOH solution between 0 and 0.3 V vs. RHE (Figs. 5e-f), probing the H-O-H bending vibration mode ($\delta_{H\text{-}O\text{-}H}$) in the 1500–1700 cm^{-1} region and the O—H stretching vibration mode in the 3000–3700 cm^{-1} range [15,19]. According to previous literature, the broad O—H stretching peak in the HOR region was deconvoluted into three peaks attributed to symmetric hydrogen-bonded (HB) water at ~3100 cm^{-1}, asymmetric HB water at ~3300 cm^{-1}, and isolated water (also known as weakly HB water) at ~3500 cm^{-1} [44,54]. Symmetric HB water reinforces the hydrogen bond network in interfacial water, which was conducive to reducing the energy barrier of the proton-coupled electron transfer process [55,56]. Consequently, symmetric HB water played a critical role in facilitating hydrogen transfer at the water-electrode interface, thereby enhancing alkaline HOR activity. We explored the interfacial water structures at HOR-relevant potential (0.2 V vs. RHE). As shown in **Fig. S14**, Ru/Cu_3P-MoP exhibited a significantly higher proportion of symmetric HB water than Ru/Cu_3P, which was key to its improved HOR performance.

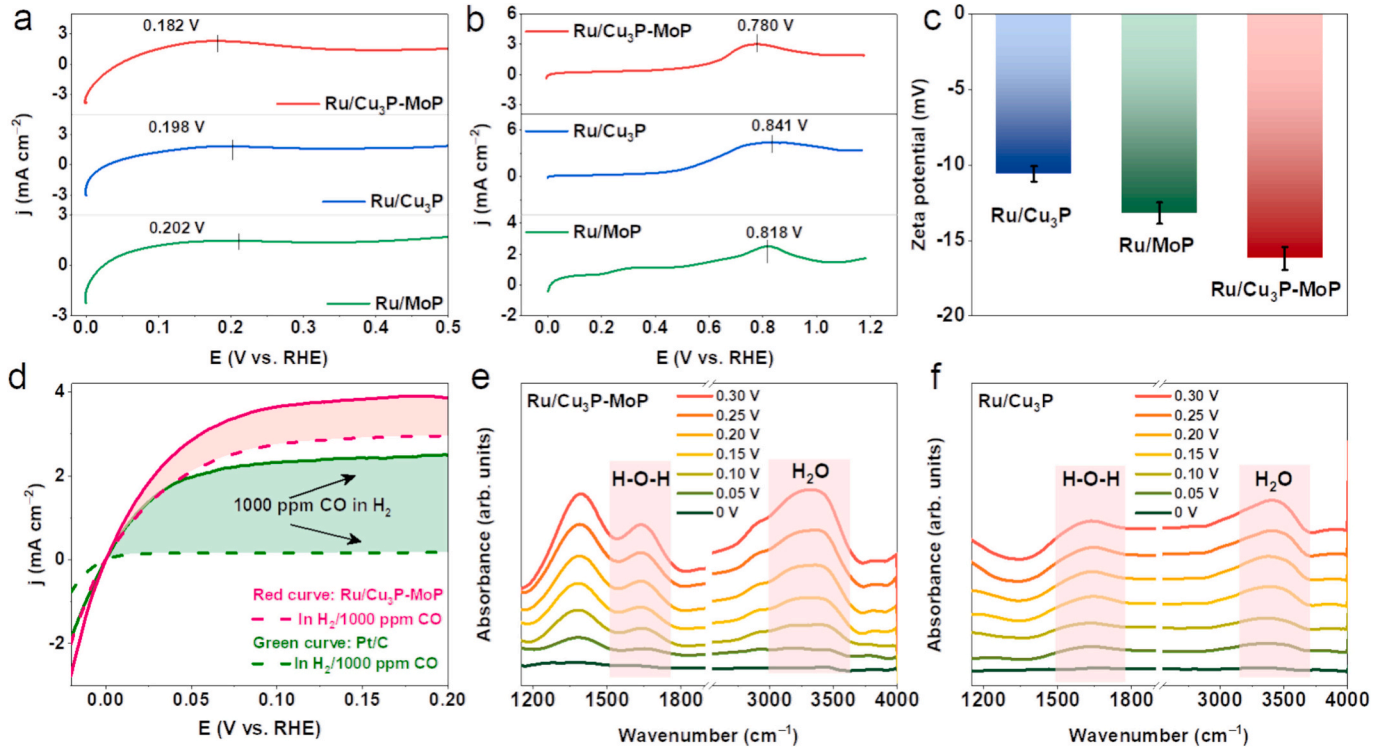

Fig. 5. (a) CV curves, (b) CO stripping curves and (c) zeta potential of Ru/Cu_3P, Ru/MoP and Ru/Cu_3P-MoP. (d) HOR polarization curves of Ru/Cu_3P-MoP and Pt/C in H_2-saturated 0.1 M KOH containing 1000 ppm CO. Interfacial water signals for ATR-SEIRAS of (e) Ru/Cu_3P-MoP and (f) Ru/Cu_3P.

3.3. Theoretical study

To interpret the correlation between the enhanced HOR activity and the metal-support interaction in Ru/Cu_3P-MoP, DFT calculations were performed on the optimized model structure (**Fig. S15**). As depicted in Fig. 6a, a notable charge accumulation was detected in Ru within the Ru/Cu_3P-MoP catalyst, revealing a robust charge interaction between Ru and Cu_3P-MoP support [57]. Based on the *d*-band theory, the position of the *d*-band center provided critical insights into the adsorption characteristics of intermediates on the catalyst surface, shedding light on the catalytic reaction mechanism [45]. The *d*-band center of Ru/Cu_3P-MoP (−2.02 eV) was situated between those of Ru/Cu_3P (−2.38 eV) and Ru/MoP (−1.03 eV), indicating a significant optimization of the adsorption strength for intermediates (Fig. 6b). Simultaneously, the DOS for Ru/Cu_3P-MoP shown considerably higher occupancy near the Fermi level compared to Ru/MoP and Ru/Cu_3P, which expedited the electron transport and enhanced conductivity [58]. The catalysts' HBE and OHBE were also analyzed, with the corresponding optimized structural models depicted in **Figs. S16–S17**. As shown in Fig. 6c, the HBE of Ru/Cu_3P-MoP was calculated to be −0.24 eV, closer to the desirable zero Gibbs free energy compared to Ru/Cu_3P (−0.46 eV) and Ru/MoP (−0.59 eV), favoring the acceleration of the HOR reaction process. Analogously, the calculated OHBEs of Ru/Cu_3P-MoP, Ru/Cu_3P and Ru/MoP were − 0.26, 0.34 and 0.49 eV, respectively, proving the improved OH absorption ability of Ru/Cu_3P-MoP. Additionally, the CO adsorption on Ru/Cu_3P-MoP (−0.42 eV) was obviously weaker than those of Ru/Cu_3P (−0.93 eV) and Ru/MoP (−1.11 eV) (Fig. 6d and **Fig. S18**). This finding indicated that Ru/Cu_3P-MoP possessed outstanding CO tolerance, which aligned with CO stripping measurements results [59].

The free energy diagrams of the alkaline HOR pathways for Ru/Cu_3P-MoP, Ru/Cu_3P and Ru/MoP, were plotted, alongside adsorption models for Ru/Cu_3P-MoP in different reaction steps (Figs. 6e-f). The HOR process began with spontaneous H adsorption, followed by the formation of OH* + H* and the subsequent formation and desorption of water. The water desorption steps were endothermic, identifying water formation as the potential-determining step (PDS). Ru/Cu_3P-MoP exhibited a much lower activation energy barrier (0.46 eV) for water formation compared to Ru/Cu_3P (0.62 eV) and Ru/MoP (0.71 eV). As anticipated, the Ru/Cu_3P-MoP appeared a much lower activation barrier (0.46 eV) of water formation than Ru/Cu_3P (0.62 eV) and Ru/MoP (0.71 eV), and the lower energy barrier conferred a decent HOR performance on the Ru/Cu_3P-MoP surface, which was in full agreement with the experimental results. The comprehensive results validated that the strong metal-support interaction between Ru and Cu_3P-MoP optimized the intermediates adsorption strength on Ru/Cu_3P-MoP surface, thereby accelerating the alkaline HOR kinetics.

3.4. LCA and TEA analysis

Life cycle analysis (LCA) and technoeconomic analysis (TEA) play pivotal roles in comprehensively evaluating the viability of the Ru/Cu_3P-MoP catalyst for alkaline fuel cell applications compared to the commercial Pt/C catalyst. LCA reveals significant environmental benefits of Ru/Cu_3P-MoP. Its total lifecycle greenhouse gas emissions are 23.1 tons CO_2-eq per kg catalyst, which is 27 % lower than the 23.55 tons CO_2-eq per kg of Pt/C. This reduction is mainly due to the enhanced durability of Ru/Cu_3P-MoP, which cuts down operational emissions during the fuel cell's operation. Moreover, the comparable recycling efficiency of Ru and the Cu_3P-MoP support, ranging from 70 to 85 %, also contributes to the emission reduction. Additionally, the use of less critical raw materials like copper and molybdenum in Ru/Cu_3P-MoP further mitigates the environmental impact related to resource extraction.

On the other hand, TEA highlights the remarkable economic advantages of Ru/Cu_3P-MoP. With a total lifecycle cost of $805.92 per kg catalyst, it represents an 87 % cost reduction compared to the $6055.57 per kg of Pt/C. Even considering the increased material consumption caused by the 50 % MOF synthesis efficiency, Ru/Cu_3P-MoP achieves a cost-per-performance ratio of $300.44 per mA μg^{-1}, which is 22 times

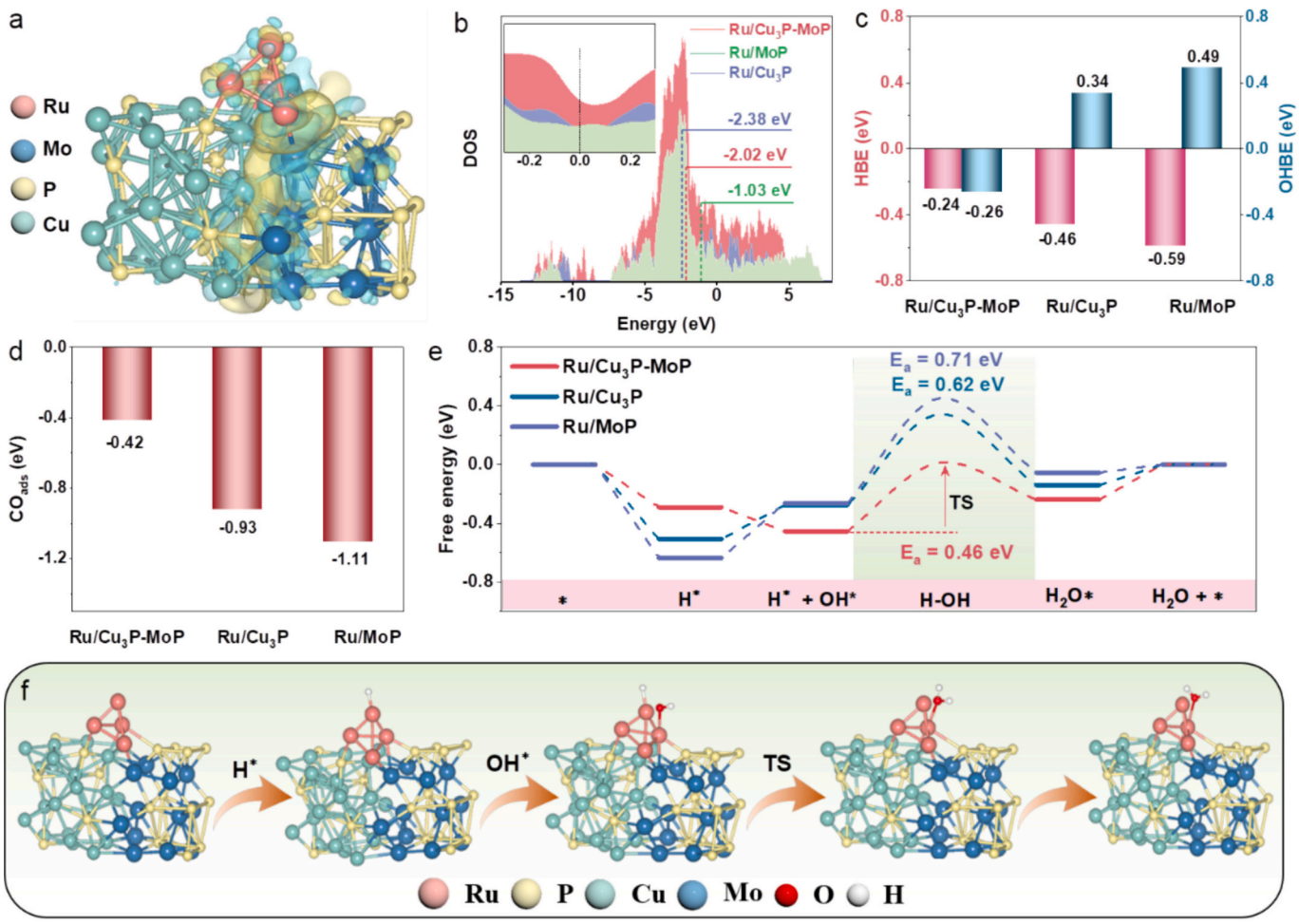

Fig. 6. (a) Charge density of Ru/Cu_3P-MoP model. (b) The density of state (DOS) plots. Calculated (c) HBEs, OHBEs and (d) CO absorption energies for Ru/Cu_3P-MoP, Ru/Cu_3P and Ru/MoP models. (e) Energetic trend of Ru/Cu_3P-MoP, Ru/Cu_3P and Ru/MoP. (f) Schematic diagram of the Ru/Cu_3P-MoP model for HOR.

more cost-effective than Pt/C ($6883.04 per mA μg^{-1}). In a word, through LCA and TEA, it becomes evident that the Ru/Cu_3P-MoP catalyst offers a dual-advantage of reduced environmental impact and cost, making it a highly sustainable and economically viable alternative to Pt/C for alkaline fuel cell applications, and paves the way for the development of more advanced and practical fuel cell technologies.

4. Conclusion

To summarize, we adopted a logical operational strategy for crafting Ru/Cu_3P-MoP electrocatalysts via a MOF self-sacrificial pyrolysis-reduction strategy, where Ru nanoparticles were secured onto the surface of Cu_3P-MoP octahedron to form an intimately contacted yolk-shell superstructure. The resulting Ru/Cu_3P-MoP hybrid surpassed other catalysts in terms of mass activity and stability. Interestingly, Ru/Cu_3P-MoP showcased a preferable resistance to CO toxicity under H_2-saturated media (containing 1000 ppm CO), manifesting its exemplary application potential. Systematic experiments illuminated that the varying work functions of Ru and Cu_3P-MoP contributed to the charge redistribution on the Ru/Cu_3P-MoP surface, resulting in a SMSI, which was instrumental in boosting charge transfer and amplifying conductivity. DFT calculations elucidated a synergistic effect between Ru and Cu_3P-MoP that adjusted the *d*-band center of Ru/Cu_3P-MoP, thereby optimizing the adsorption of intermediates and hastening the HOR reaction rate. Besides, LCA and TEA are used to evaluate Ru/Cu_3P-MoP against Pt/C for alkaline fuel cells. LCA shows 27 % lower lifecycle greenhouse gas emissions for Ru/Cu_3P-MoP, while TEA reveals an 87 % cost reduction and a 22-fold better cost -per-performance ratio. Overall, the Ru/Cu_3P-MoP catalyst not only addresses critical challenges associated with Pt-based catalysts, such as high costs, limited durability, and CO sensitivity but also represents a significant scientific advancement through the use of SMSI to enhance catalytic activity. By integrating exceptional performance metrics with substantial reductions in emissions and cost, this study establishes Ru/Cu_3P-MoP as a promising solution for advancing sustainable and scalable alkaline fuel cell technologies.

CRediT authorship contribution statement

Shuqing Zhou: Writing – original draft, Methodology. **Yi Liu:** Writing – original draft. **Chenggong Niu:** Validation, Investigation. **Jingya Guo:** Validation. **Tayirjan Taylor Isimjan:** Writing – review & editing. **Jianniao Tian:** Writing – review & editing, Supervision. **Xiulin Yang:** Writing – review & editing, Supervision.

Declaration of competing interest

The authors declare that they have no known competing financial interests or personal relationships that could have appeared to influence the work reported in this paper.

Acknowledgements

This work has been supported by the National Natural Science

Foundation of China (no. 52363028 and 21,965,005), Natural Science Foundation of Guangxi Province (2021GXNSFAA076001), Guangxi Technology Base and Talent Subject (GUIKE AD23023004 and GUIKE AD20297039).

Appendix A. Supplementary data

Supplementary data to this article can be found online at https://doi.org/10.1016/j.cej.2025.167732.

Data availability

The data that has been used is confidential.

References

[1] Y. Feng, S. Lu, L. Fu, F. Yang, L. Feng, Alleviating the competitive adsorption of hydrogen and hydroxyl intermediates on Ru by d–p orbital hybridization for hydrogen electrooxidation, Chem. Sci. 15 (2024) 2123–2132, https://doi.org/10.1039/d3sc05387c.

[2] L. Xing, S. Du, R. Chen, M. Mamlouk, K. Scott, Anode partial flooding modelling of proton exchange membrane fuel cells: model development and validation, Energy 96 (2016) 80–95, https://doi.org/10.1016/j.energy.2015.12.048.

[3] S. Liu, Y. Wang, T. Jiang, S. Jin, M. Sajid, Z. Zhang, J. Xu, Y. Fan, X. Wang, J. Chen, Z. Liu, X. Zheng, K. Zhang, Q. Nian, Z. Zhu, Q. Peng, T. Ahmad, K. Li, W. Chen, Non-Noble metal high-entropy alloy-based catalytic electrode for long-life hydrogen gas batteries, ACS Nano 18 (2024) 4229–4240, https://doi.org/10.1021/acsnano.3c09482.

[4] Y. Zhao, F. Yang, W. Zhang, Q. Li, X. Wang, L. Su, X. Hu, Y. Wang, Z. Wang, L. Zhuang, S. Chen, W. Luo, High-performance Ru_2P anodic catalyst for alkaline polymer electrolyte fuel cells, CCS Chem. 4 (2021) 1732–1744, https://doi.org/10.31635/ccschem.021.202100810.

[5] B. Wang, Y. Cheng, H. Su, M. Cheng, Y. Li, H. Geng, Z. Dai, Boosting Transport Kinetics of Cobalt Sulfides Yolk–Shell Spheres by Anion Doping for Advanced Lithium and Sodium Storage, ChemSusChem 13 (2020) 4078–4085, https://doi.org/10.1002/cssc.202001261.

[6] Z. Cheng, Y. Yang, P. Wang, P. Wang, J. Yang, D. Wang, Q. Chen, Optimizing Hydrogen and Hydroxyl Adsorption over $Ru/WO_{2.9}$ Metal/Metalloid Heterostructure Electrocatalysts for Highly Efficient and Stable Hydrogen Oxidation Reactions in Alkaline Media, Small 20 (2024), https://doi.org/10.1002/smll.202307780, 2307780.

[7] H. Zhao, D. Chen, R. Yu, J. Jiao, W. Zeng, J. Zhu, X. Mu, Y. Yao, D. Wu, Y. Zhang, J. Wu, S. Mu, Atomizing platinum for hydrogen electrode reactions, Nano Energy 121 (2024) 109247, https://doi.org/10.1016/j.nanoen.2023.109247.

[8] D. Strmcnik, M. Uchimura, C. Wang, R. Subbaraman, N. Danilovic, D. van der Vliet, A.P. Paulikas, V.R. Stamenkovic, N.M. Markovic, Improving the hydrogen oxidation reaction rate by promotion of hydroxyl adsorption, Nat. Chem. 5 (2013) 300–306, https://doi.org/10.1038/nchem.1574.

[9] L. Wei, N. Fang, F. Xue, S. Liu, W.-H. Huang, C.-W. Pao, Z. Hu, Y. Xu, H. Geng, X. Huang, Amorphous–crystalline RuTi nanosheets enhancing OH species adsorption for efficient hydrogen oxidation catalysis, Chem. Sci. 15 (2024) 3928–3935, https://doi.org/10.1039/d3sc06705j.

[10] M.T.M. Koper, A basic solution, Nat. Chem. 5 (2013) 255–256, https://doi.org/10.1038/nchem.1600.

[11] W. Ni, J.L. Meibom, N.U. Hassan, M. Chang, Y.-C. Chu, A. Krammer, S. Sun, Y. Zheng, L. Bai, W. Ma, S. Lee, S. Jin, J.S. Luterbacher, A. Schüler, H.M. Chen, W. E. Mustain, X. Hu, Synergistic interactions between PtRu catalyst and nitrogen-doped carbon support boost hydrogen oxidation, Nat. Catal. 6 (2023) 773–783, https://doi.org/10.1038/s41929-023-01007-1.

[12] H. Wang, H.D. Abruña, IrPdRu/C as H_2 oxidation catalysts for alkaline fuel cells, J. Am. Chem. Soc. 139 (2017) 6807–6810, https://doi.org/10.1021/jacs.7b02434.

[13] W. Li, D. Wang, Y. Zhang, L. Tao, T. Wang, Y. Zou, Y. Wang, R. Chen, S. Wang, Defect engineering for fuel-cell Electrocatalysts, Adv. Mater. 32 (2020) 1907879, https://doi.org/10.1002/adma.201907879.

[14] W. Luo, X. Wang, L. Zhao, Y. Tong, Y. Zhen, Y. Cui, P. Liu, T. Cai, Z. Yan, Q. Xue, S. G. Mohamed, X. Li, X. Yuan, W. Xing, Modulating dual-active sites within one ruthenium nanocluster by engineering electronic metal-support interactions for efficient hydrogen electro-oxidation, Chem. Eng. J. 498 (2024) 155107, https://doi.org/10.1016/j.cej.2024.155107.

[15] L. Li, F. Tian, F. Wu, L. Qiu, S. Geng, M. Li, Z. Chen, W. Yang, Y. Liu, Y. Yu, Strong electronic metal-support interaction of $Ni_4Mo/N\text{-}SrMoO_4$ promotes alkaline hydrogen electrocatalysis, Appl. Catal. B Environ. Energy 361 (2025) 124660, https://doi.org/10.1016/j.apcatb.2024.124660.

[16] X. Wang, X. Liu, S. Wu, K. Liu, X. Meng, B. Li, J. Lai, L. Wang, S. Feng, Phosphorus vacancies enriched cobalt phosphide embedded in nitrogen doped carbon matrix enabling seawater splitting at ampere-level current density, Nano Energy 109 (2023) 108292, https://doi.org/10.1016/j.nanoen.2023.108292.

[17] X. Qin, B. Yan, D. Kim, Z. Teng, T. Chen, J. Choi, L. Xu, Y. Piao, Interfacial engineering and hydrophilic/aerophobic tuning of Sn_4P_3/Co_2P heterojunction nanoarrays for high-efficiency fully reversible water electrolysis, Appl. Catal. B Environ. 304 (2022) 120923, https://doi.org/10.1016/j.apcatb.2021.120923.

[18] Y. Pi, Z. Qiu, Y. Sun, H. Ishii, Y.F. Liao, X. Zhang, H.Y. Chen, H. Pang, Synergistic mechanism of sub-Nanometric Ru clusters anchored on tungsten oxide nanowires for high-efficient bifunctional hydrogen Electrocatalysis, Adv. Sci. 10 (2023) 2206096, https://doi.org/10.1002/advs.202206096.

[19] X. Mu, X. Zhang, Z. Chen, Y. Gao, M. Yu, D. Chen, H. Pan, S. Liu, D. Wang, S. Mu, Constructing symmetry-mismatched $RuxFe_{3-x}O_4$ Heterointerface-supported Ru clusters for efficient hydrogen evolution and oxidation reactions, Nano Lett. 24 (2024) 1015–1023, https://doi.org/10.1021/acs.nanolett.3c04690.

[20] M. Guo, M. Xu, Y. Qu, C. Hu, P. Yan, T.T. Isimjan, X. Yang, Electronic/mass transport increased hollow porous Cu_3P/MoP nanospheres with strong electronic interaction for promoting oxygen reduction in Zn-air batteries, Appl. Catal. B Environ. 297 (2021) 120415, https://doi.org/10.1016/j.apcatb.2021.120415.

[21] Y. Song, X. Xin, S. Guo, Y. Zhang, L. Yang, B. Wang, X. Li, One-step MOFs-assisted synthesis of intimate contact MoP-Cu_3P hybrids for photocatalytic water splitting, Chem. Eng. J. 384 (2020) 123337, https://doi.org/10.1016/j.cej.2019.123337.

[22] H.B. Wu, B.Y. Xia, L. Yu, X.-Y. Yu, X.W. Lou, Porous molybdenum carbide nano-octahedrons synthesized via confined carburization in metal-organic frameworks for efficient hydrogen production, Nat. Commun. 6 (2015), https://doi.org/10.1038/ncomms7512.

[23] Y. Yang, Y. Huang, S. Zhou, Y. Liu, L. Shi, T.T. Isimjan, X. Yang, Delicate surface vacancies engineering of Ru doped MOF-derived Ni-NiO@C hollow microsphere superstructure to achieve outstanding hydrogen oxidation performance, J. Energy Chem. 72 (2022) 395–404, https://doi.org/10.1016/j.jechem.2022.06.011.

[24] H. Yu, X. Han, Z. Hua, W. Yang, X. Wu, Y. Wu, S. Chen, W. Hong, S. Deng, J. Zhang, J. Wang, Modulating electronic properties of carbon for selective electrochemical reduction of CO_2 to methanol on Cu_3P@C, ACS Catal. 14 (2024) 12783–12791, https://doi.org/10.1021/acscatal.4c02465.

[25] J. Zheng, W. Zhang, J. Hu, Y. Xie, Y. Lai, B. Hong, K. Zhang, Z. Zhang, Highly dispersed MoP encapsulated in P-doped porous carbon boosts polysulfide redox kinetics of lithium-sulfur batteries, Mater. Today Energy 18 (2020) 100531, https://doi.org/10.1016/j.mtener.2020.100531.

[26] K. Cao, X.-X. Qu, H. Jiang, Y.-H. Su, C. Zhang, G. Frapper, Pressure-Induced Novel Stable Stoichiometries in Molybdenum–Phosphorus Phase Diagrams under Pressure, J. Phys. Chem. C 123 (2019) 30187–30197, https://doi.org/10.1021/acs.jpcc.9b09466.

[27] J. Wang, C. Hu, L. Wang, Y. Yuan, K. Zhu, Q. Zhang, L. Yang, J. Lu, Z. Bai, Suppressing thermal migration by fine-tuned metal-support interaction of Iron single-atom catalyst for efficient ORR, Adv. Funct. Mater. 33 (2023) 202304277, https://doi.org/10.1002/adfm.202304277.

[28] J. Zhang, C. Wang, S. Lu, S. Liu, P. Liang, H. Yi, M. Li, M. Jin, R. Wang, G. Jiang, Reactant enrichment in yolk-shell structured Pd/TiN nanoreactors for boosting electrocatalytic hydrodechlorination performance, Chem. Eng. J. 481 (2024) 148325, https://doi.org/10.1016/j.cej.2023.148325.

[29] Y. Liu, X. Li, Q. Zhang, W. Li, Y. Xie, H. Liu, L. Shang, Z. Liu, Z. Chen, L. Gu, Z. Tang, T. Zhang, S. Lu, A general route to prepare low-ruthenium-content bimetallic Electrocatalysts for pH-universal hydrogen evolution reaction by using carbon quantum dots, Angew. Chem. Int. Ed. 59 (2020) 1718–1726, https://doi.org/10.1002/anie.201913910.

[30] H. Song, Y. Li, L. Shang, Z. Tang, T. Zhang, S. Lu, Designed controllable nitrogen-doped carbon-dots-loaded MoP nanoparticles for boosting hydrogen evolution reaction in alkaline medium, Nano Energy 72 (2020) 104730, https://doi.org/10.1016/j.nanoen.2020.104730.

[31] H. Shi, Y. Yang, P. Meng, J. Yang, W. Zheng, P. Wang, Y. Zhang, X. Chen, Z. Cheng, C. Zong, D. Wang, Q. Chen, Local charge transfer unveils Antideactivation of Ru at high potentials for the alkaline hydrogen oxidation reaction, J. Am. Chem. Soc. 146 (2024) 16619–16629, https://doi.org/10.1021/jacs.4c03622.

[32] M. Guo, L.X. Wang, Z.Y. Huang, H.T. Li, T.T. Isimjan, X.L. Yang, Modulating the energy barrier via the synergism of CuP and CoP to accelerate kinetics for bolstering oxygen electrocatalysis in Zn-air batteries, ACS Nano 18 (2024) 17901–17912, https://doi.org/10.1021/acsnano.4c04479.

[33] J. Zhu, J. Chi, T. Cui, L. Guo, S. Wu, B. Li, J. Lai, L. Wang, F doping and P vacancy engineered FeCoP nanosheets for efficient and stable seawater electrolysis at large current density, Appl. Catal. Environ 328 (2023) 122487, https://doi.org/10.1016/j.apcatb.2023.122487.

[34] L. Jing, G. Jie, W. Yu, H. Ren, X. Cui, X. Chen, L. Jiang, A unique sandwich-structured Ru-TiO/TiO_2@NC as an efficient bi-functional catalyst for hydrogen oxidation and hydrogen evolution reactions, Chem. Eng. J. 472 (2023) 145009, https://doi.org/10.1016/j.cej.2023.145009.

[35] M. Liu, B.A. Lu, G. Yang, P. Yuan, H. Xia, Y. Wang, K. Guo, S. Zhao, J. Liu, Y. Yu, W. Yan, C.L. Dong, J.N. Zhang, S. Mu, Concave Pt–Zn nanocubes with high-index faceted Pt skin as highly efficient oxygen reduction catalyst, Adv. Sci. 9 (2022) 2200147, https://doi.org/10.1002/advs.202200147.

[36] L. Su, X. Fan, Y. Jin, H. Cong, W. Luo, Hydroxyl-binding energy-induced kinetic gap narrowing between acidic and alkaline hydrogen oxidation reaction on intermetallic Ru_3Sn_7 catalyst, Small 19 (2023) 2207603, https://doi.org/10.1002/smll.202207603.

[37] Z. Chen, Y. Song, J. Cai, X. Zheng, D. Han, Y. Wu, Y. Zang, S. Niu, Y. Liu, J. Zhu, X. Liu, G. Wang, Tailoring the d-band centers enables Co_4N Nanosheets to be highly active for hydrogen evolution catalysis, Angew. Chem. Int. Ed. 57 (2018) 5076–5080, https://doi.org/10.1002/anie.201801834.

[38] Y. Li, C. Yang, J. Yue, H. Cong, W. Luo, Polymorphism-interface-induced work function regulating on Ru nanocatalyst for enhanced alkaline hydrogen oxidation reaction, Adv. Funct. Mater. 33 (2023) 2211586, https://doi.org/10.1002/adfm.202211586.

[39] X. Zhang, L. Xia, G. Zhao, B. Zhang, Y. Chen, J. Chen, M. Gao, Y. Jiang, Y. Liu, H. Pan, W. Sun, Fast and Durable Alkaline Hydrogen Oxidation Reaction at the

Electron-Deficient Ruthenium–Ruthenium Oxide Interface, Adv. Mater. 35 (2023) 2208821, https://doi.org/10.1002/adma.202208821.
[40] Y.Y. Guo, W.D. He, X.H. Tan, Y.H. Xiao, B.J. Du, C.H. Wang, H. Cui, Y. Li, C. X. Wang, Promoting the Volmer step of alkaline hydrogen oxidation reaction by incorporating Zn single atoms into Ru lattice and carbon frameworks, Adv. Funct. Mater. 2412142 (2024), https://doi.org/10.1002/adfm.202412142.
[41] Y. Yang, L. Zhao, Y. Sun, Y. Lin, L. Yang, K. Mao, C. Li, K. Xu, Tuning Electron transfer in atomic-scale Pt-supported catalysts for the alkaline hydrogen oxidation reaction, Inorg. Chem. 62 (2023) 5032–5039, https://doi.org/10.1021/acs.inorgchem.3c00293.
[42] S. Zhou, Y. Liu, C. Niu, T.T. Isimjan, J. Tian, X. Yang, Lattice strain engineering of Ni-doped Pd nanoparticles: realizing efficient and CO-resistant alkaline hydrogen oxidation, Renew. Energy 240 (2025) 122242, https://doi.org/10.1016/j.renene.2024.122242.
[43] L.X. Su, Y.M. Jin, X.R. Fan, Z.Y. Liu, W. Luo, pH-dependent binding energy-induced inflection-point behaviors for pH-universal hydrogen oxidation reaction, Sci. China Chem. 66 (2023) 3262–3268, https://doi.org/10.1007/s11426-023-1709-0.
[44] C. Yang, J. Yue, G. Wang, W. Luo, Activating and identifying the active site of RuS_2 for alkaline hydrogen oxidation Electrocatalysis, Angew. Chem. Int. Ed. 62 (2024) e202401453, https://doi.org/10.1002/anie.202401453.
[45] L. Su, Y. Jin, D. Gong, X. Ge, W. Zhang, X. Fan, W. Luo, The role of discrepant reactive intermediates on Ru-Ru_2P Heterostructure for pH-universal hydrogen oxidation reaction, Angew. Chem. Int. Ed. 62 (2023) e202215585, https://doi.org/10.1002/anie.202215585.
[46] L. Wang, S. Meng, C. Tang, C. Zhan, S. Geng, K. Jiang, X. Huang, L. Bu, PtNi/PtIn-skin fishbone-like nanowires boost alkaline hydrogen oxidation catalysis, ACS Nano 17 (2023) 17779–17789, https://doi.org/10.1021/acsnano.3c02832.
[47] C. Yang, Y. Li, J. Yue, H. Cong, W. Luo, Promoting water formation in sulphate-functionalized Ru for efficient hydrogen oxidation reaction under alkaline electrolytes, Chem. Sci. 14 (2023) 6289–6294, https://doi.org/10.1039/d3sc02144k.
[48] Y. Men, D. Wu, Y. Hu, L. Li, P. Li, S. Jia, J. Wang, G. Cheng, S. Chen, W. Luo, Understanding alkaline hydrogen oxidation reaction on PdNiRuIrRh high-entropy-alloy by machine learning potential, Angew. Chem. Int. Ed. 62 (2023) e202217976, https://doi.org/10.1002/anie.202217976.
[49] Z. Cui, Z. Ren, C. Ma, B. Chen, G. Chen, R. Lu, W. Zhu, T. Gan, Z. Wang, Z. Zhuang, Y. Han, Dilute RuCo alloy synergizing single Ru and co atoms as efficient and CO-resistant anode catalyst for anion exchange membrane fuel cells, Angew. Chem. Int. Ed. 63 (2024) e202404761, https://doi.org/10.1002/anie.202404761.
[50] L. Wang, Z. Xu, C.-H. Kuo, J. Peng, F. Hu, L. Li, H.-Y. Chen, J. Wang, S. Peng, Stabilizing low-valence single atoms by constructing metalloid tungsten carbide supports for efficient hydrogen oxidation and evolution, Angew. Chem. Int. Ed. 62 (2023) e202311937, https://doi.org/10.1002/anie.202311937.
[51] H. Luo, K. Wang, F. Lin, F. Lv, J. Zhou, W. Zhang, D. Wang, W. Zhang, Q. Zhang, L. Gu, M. Luo, S. Guo, Amorphous MoOx with high oxophilicity interfaced with PtMo alloy nanoparticles boosts anti-CO hydrogen electrocatalysis, Adv. Mater. 35 (2023) 2211854, https://doi.org/10.1002/adma.202211854.
[52] J.-T. Ren, D. Yang, L. Chen, Z.-Y. Yuan, Vanadium-doped Heterointerfaced Ni_3N-MoO_x Nanosheets with optimized H and H_2O adsorption for effective alkaline hydrogen Electrocatalysis, Small 20 (2024) 2406335, https://doi.org/10.1002/smll.202406335.
[53] Y. Huang, X. Li, P.K. Shen, C. Yang, J. Zhu, High-performance MoP-Mo_2C/C heterogeneous nanoparticle catalysts for alkaline hydrogen evolution and oxidation reactions, ACS Mater. Lett. 6 (2024) 1678–1685, https://doi.org/10.1021/acsmaterialslett.3c01494.
[54] Y. Men, Y. Tan, P. Li, Y.L. Jiang, L. Li, X.Z. Su, X. Men, X.P. Sun, S.L. Chen, W. Luo, Boosting alkaline hydrogen oxidation kinetics through interfacial environments induced surface migration of adsorbed hydroxyl, Angew. Chem. Int. Ed. 63 (2024) e202411341, https://doi.org/10.1002/anie.202411341.
[55] L. Wei, Y. Dong, W. Yan, Y. Zhang, C. Zhan, W.-H. Huang, C.-W. Pao, Z. Hu, H. Lin, Y. Xu, H. Geng, X. Huang, Hollow Pt-encrusted RuCu Nanocages optimizing OH adsorption for efficient hydrogen oxidation Electrocatalysis, Angew. Chem. Int. Ed. 64 (2025) e202420177, https://doi.org/10.1002/anie.202420177.
[56] Y. Jin, X. Fan, W. Cheng, Y. Zhou, L. Xiao, W. Luo, The role of phosphorus on alkaline hydrogen oxidation electrocatalysis for ruthenium phosphides, Angew. Chem. Int. Ed. 63 (2024) e202406888, https://doi.org/10.1002/anie.202406888.
[57] J. Yang, W. Li, D. Wang, Y. Li, Electronic Metal–Support Interaction of Single-Atom Catalysts and Applications in Electrocatalysis, Adv. Mater. 32 (2020) 2003300, https://doi.org/10.1002/adma.202003300.
[58] J. Yue, Y. Li, C. Yang, W. Luo, Hydroxyl-binding induced hydrogen bond network connectivity on Ru-based catalysts for efficient alkaline hydrogen oxidation Electrocatalysis, Angew. Chem. Int. Ed. e202415447 (2024), https://doi.org/10.1002/anie.202415447.
[59] Y. Liu, L. Cheng, S. Zhou, C. Niu, T.T. Isimjan, X. Yang, Built-in electric field-driven electron transfer behavior at Ru-RuP_2 heterointerface fosters efficient and CO-resilient alkaline hydrogen oxidation, Appl. Catal. B Environ. Energy 362 (2025) 124709, https://doi.org/10.1016/j.apcatb.2024.124709.